

Supplementary Information for

Strain Engineering Coupled with Optical Regulation towards High-sensitivity In₂S₃ Photodetector

Jianting Lu^{1†}, Jiandong Yao^{2†}, Jiahao Yan³, Wei Gao¹, Le Huang¹, Zhaoqiang Zheng^{1, 4*}, Menglong Zhang⁵, Jingbo Li^{5, 6*}

¹ School of Materials and Energy, Guangdong University of Technology, Guangzhou, 510006, Guangdong, P. R. China.

² State Key Laboratory of Optoelectronic Materials and Technologies, Nanotechnology Research Center, School of Materials Science & Engineering, Sun Yat-sen University, Guangzhou, 510275, Guangdong, P. R. China.

³ Institute of Nanophotonics, Jinan University, Guangzhou, 511443, Guangdong, P. R. China.

⁴ Department of Electronic Engineering, The Chinese University of Hong Kong, Hong Kong SAR, P. R. China.

⁵ Institute of Semiconductors, South China Normal University, Guangzhou, 510631, Guangdong, P. R. China.

⁶ State Key Laboratory for Superlattices and Microstructures, Institute of Semiconductors, Chinese Academy of Sciences, Beijing, 100083, P. R. China.

† These authors contributed equally to this work.

*Corresponding authors: zhengzhq5@mail2.sysu.edu.cn and jbli@semi.ac.cn

Supplementary Notes

Supplementary Note 1: Synthesis of 2D In₂S₃ flakes

The growth of 2D In₂S₃ flakes was carried out in a horizontal quartz tube furnace with a single heating zone. In₂S₃ power (99.999%, Alfa Aesar) was placed at the center of the hot zone, while the fluorophlogopite mica substrate was positioned downstream about 5 cm away from the In₂S₃ power. Firstly, the tube was purged with 400 sccm ultrahigh purity argon (Ar) gas (99.999%) for 15 min to provide an inner environment. Then, ultrahigh purity Ar gas with flow rates of 20–30 sccm was introduced into the quartz tube as the carrier gas. Under ambient pressure, the growth temperature was set at 980 °C and the growth time was 5 min. Finally, the furnace was naturally cooled to room temperature under 100–200 sccm ultrahigh purity Ar gas.

Supplementary Note 2: Calculation of surface potential difference (SPD):

The SPD between the AFM tip and In₂S₃ can be calculated as follows:

$$e\text{SPD}_{\text{In}_2\text{S}_3} = W_{\text{tip}} - W_{\text{In}_2\text{S}_3}$$

$$e\text{SPD}_{\text{NGs-In}_2\text{S}_3} = W_{\text{tip}} - W_{\text{NGs-In}_2\text{S}_3}$$

where e , $W_{\text{NGs-In}_2\text{S}_3}$, $W_{\text{In}_2\text{S}_3}$ and W_{tip} represent electron charge, work functions of NGs-In₂S₃, In₂S₃ and AFM tip, respectively¹. Thus, the Fermi level difference (ΔE_f) between NGs-In₂S₃ and In₂S₃ can be obtained by

$$\Delta E_f = W_{\text{NGs-In}_2\text{S}_3} - W_{\text{In}_2\text{S}_3} = e\text{SPD}_{\text{In}_2\text{S}_3} - e\text{SPD}_{\text{NGs-In}_2\text{S}_3}$$

Supplementary Note 3: FDTD Simulations

The scattering spectra near-field distributions were calculated using the finite-difference time domain method (FDTD Solutions 8.6.0, Lumerical Solutions, Inc.). The normal incident total-field scattered-field plane wave at the visible wavelengths (300–900 nm) combined with planar detectors was used to simulate the reflection spectra and the electric field distributions. The SiO₂ NGs were illuminated by a plane wave with linear polarization (along x axis). The size parameters were set according to the SEM images. A mesh size of 2 nm for the illuminated region was used.

Supplementary Note 4: Calculation of Performance Parameters

To better compare the performance of photodetectors with different sizes and operating conditions, several figures of merit are defined.

Responsivity (R):

Photoresponsivity is defined as the ratio of the photocurrent to the incident light power on the active region of the device, which can be expressed as:

$$R = I_{ph}/(PS)$$

where I_{ph} is the photocurrent ($I_{ph} = I_{light} - I_d$), P is the light power density, S is the effective area under incident light, and I_{light} and I_d are the device current under light and dark²⁻³.

Detectivity (D*):

The detectivity is a useful parameter for comparing the detection performance of photodetectors with different materials and geometries⁴⁻⁵. Moreover, the detectivity can truly reflect the capability of a device to detect weak light signals, and it is a commonly adapted figure of merit to quantify the sensitivity of a photodetector with respect to noise^{2, 6}. D^* is defined as⁷:

$$D^* = (Sf_B)^{1/2}/NEP$$

where e is the electronic charge, f_B is the electrical bandwidth, NEP is the noise equivalent power, which corresponds to the incident power required for the signal-to-noise ratio (SNR) to be unity in a 1 Hz bandwidth⁸. A commonly-accepted assumption is that the shot noise from dark current is the dominant contribution^{6, 9}. Based on this assumption, the NEP can be approximated as:

$$NEP = (2eI_{\text{dark}})^{1/2}/R$$

Thus, D^* can be expressed as

$$D^* = S^{1/2}R/(2eI_{\text{dark}})^{1/2}$$

Signal-to-Noise Ratio (SNR):

Low noise is a significant factor for a photodetector because it ultimately determines the lowest detectable signal strength. Noise always exists in a photodetection process, which limits the detection of small amounts of radiation energy by producing a random fluctuation in the output of the device. Higher SNR means fewer disturbances from the background noise¹⁰⁻¹¹. The SNR of a photodetector is expressed as

$$SNR = I_{\text{ph}}/I_{\text{d}}$$

Photoconductive Gain (G):

Photoconductive gain is used to evaluate the ability of generating multiple carriers by a single incident photon. It is given as:

$$G = (hcR)/(e\lambda\eta)$$

where h is the Planck constant, c is the light velocity, λ is the excitation wavelength, and η is external quantum efficiency (assuming 100%)²⁻³.

Response Time (τ_{rise}) and Recovery Time (τ_{decay}):

The response time and recovery time are defined as the time interval required from 0%/100% to 90%/10% of the net photocurrent¹².

Supplementary Figures

Figure S1. Schematic diagrams showing the fabrication process of the In_2S_3 photodetector.

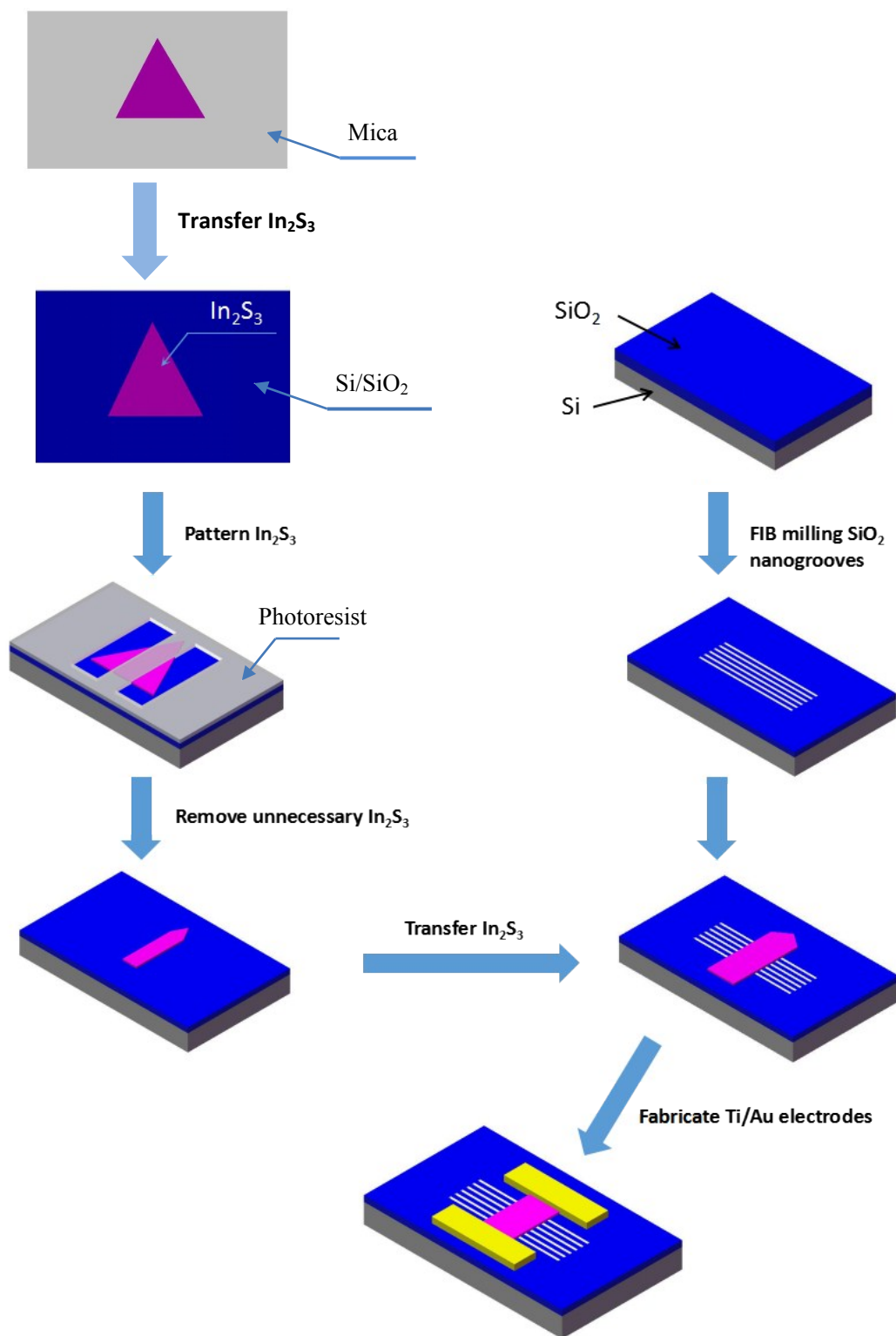
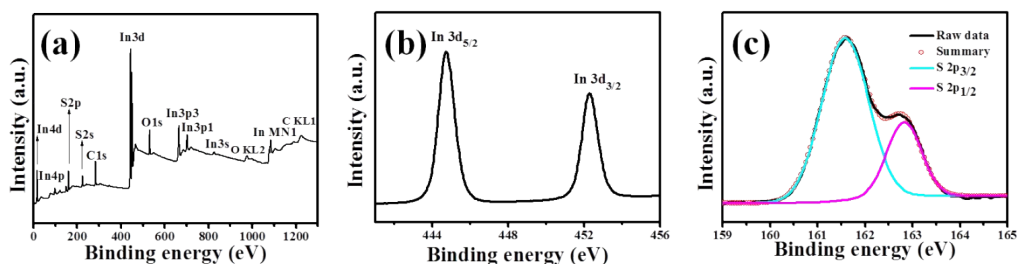


Figure S2. XPS pattern of In_2S_3 . (a) Full spectrum of In_2S_3 . Core spectra of (b) In 3d and (c) S 2p.



The full scan in Figure S2(a) verifies that the sample just consists of In and S elements. Therefore, the fabricated In_2S_3 nanoflakes manifest high chemical purity, revealing the feasibility of directly preparing high quality In_2S_3 crystals. High resolution scans of In 3d and S 2p are also recorded in Figure S2(b–c), respectively. The peaks located at 444.75 and 452.3 eV can be assigned to In $3d_{5/2}$ and In $3d_{3/2}$, respectively. Correspondingly, the peaks at 161.6 and 162.7 eV in the S 2p spectrum are indexed to S $2p_{3/2}$ and S $2p_{1/2}$, respectively. These peaks are consistent with the reported values of In_2S_3 ¹³. Moreover, the atomic molar ratio of In to S is 2: 3, matching well with its stoichiometric ratio.

Figure S3. Schematic diagram and structural parameters of the SiO₂ nanogroove array.

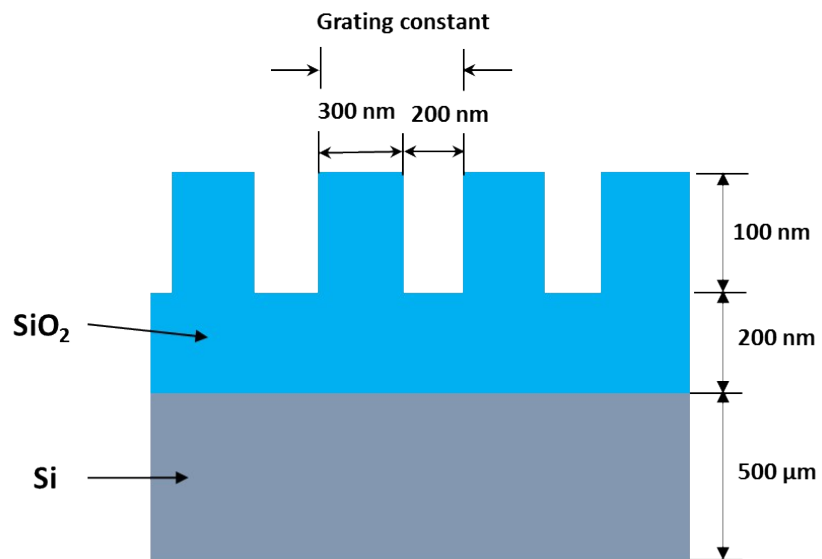


Figure S4. Enlarged SEM images of the other two types of SiO₂ NGs with grating constants of (a) 300 nm and (b) 700 nm. (c–f) Calculated field intensity (E^2) profiles with respect to x-z plane of the SiO₂ NGs with different grating constants.

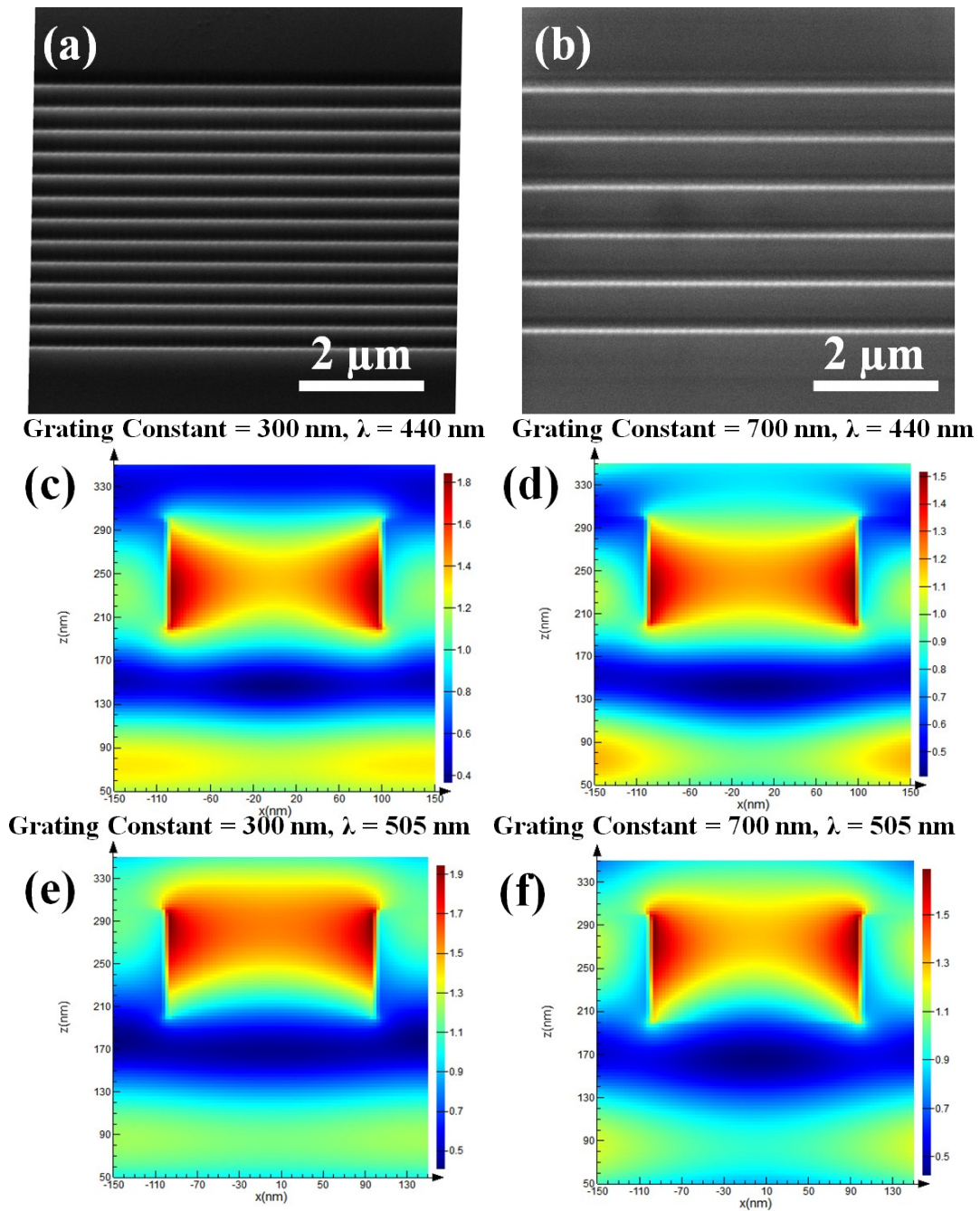
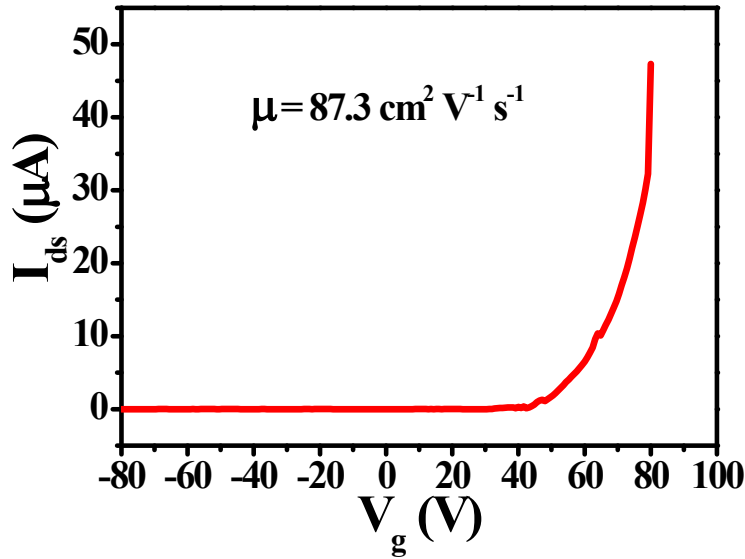


Figure S5. Transfer curve of a f-In₂S₃ device.



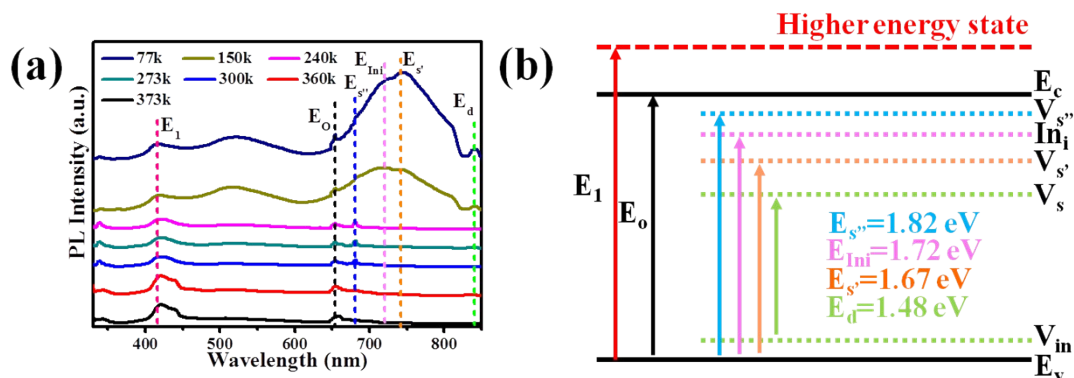
The electron mobility can be acquired by the following equation¹⁴⁻¹⁵

$$\mu = \frac{\partial I_{ds}}{\partial V_g} \left(\frac{Ld}{W\varepsilon_0\varepsilon_r V_{ds}} \right)$$

where L and W are the length and width of the channel, $\frac{\partial I_{ds}}{\partial V_g}$ is slope of the transfer curve, μ is mobility, ε_r is the relative static permittivity, ε_0 is the electric constant, and d is the thickness of the SiO₂ layer, V_{ds} is the source-drain voltage. Herein, $V_{ds} = 2$ V,

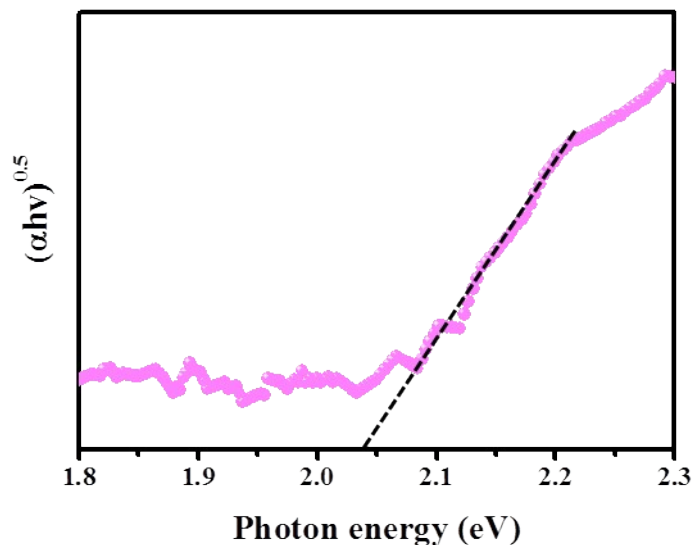
$L = 2$ μm , $W = 15$ μm , and $d = 300$ nm. Then, $\varepsilon_0 = 8.85 \times 10^{-12}$ F/m, $\varepsilon_r = 3.9$, and $\frac{\partial I_{ds}}{\partial V_g} = 1.51 \times 10^{-5}$ A/V. Based on the data above, the electron mobility is calculated to be $87.3 \text{ cm}^2 \text{ V}^{-1} \text{ s}^{-1}$.

Figure S6. (a) Temperature-dependent PL spectra of In_2S_3 in the temperature range of 77–373 K. (b) The illustration of probable band structure of In_2S_3 nanoflake.



A broad and multiemission at longer wavelength arises and becomes stronger as the temperature decreases (Figure S6(a)). A peak at ~ 650 nm (1.91 eV) was found at the spectrum, which can be assigned to the bandgap energy of In_2S_3 ¹⁶. Another peak at ~ 410 nm (~ 3 eV) was found at the spectrum, which can be assigned to the transition to higher energy state of In_2S_3 ¹⁷. Four peaks located at about 680 nm (1.82 eV), 720 nm (1.72 eV), 742 nm (1.67 eV) and 837 nm (1.48 eV) can be found in lower energy range, which exhibit nearly temperature-invariant character of energy shift. In several previous studies, many energy states coming from vacancy, self-interstitial and antisite defects have been theoretically predicted and experimentally investigated¹⁷⁻²⁰. The dangling bonds by vacancies are not sensitive to the thermal expansion of lattice when the temperature is changed²¹. These vacancies in the In_2S_3 unit cell include S vacancies (V_S), In vacancies (V_{In}) and In interstitial vacancy (In_i). The S vacancies and In interstitial act as donors, while the In vacancies act as acceptors²². According to the energy level reported by earlier reports, the four defect emissions of the In_2S_3 nanoflake should originate from the recombination of $V_{S''}$ to E_v (1.82 eV), In_i to E_v (1.72 eV), $V_{S'}$ to E_v (1.67 eV) and V_S to V_{In} (1.48 eV), respectively, where $V_{S'}$ and $V_{S''}$ are the higher defect levels of S vacancies. Based on the above discussion, all the probable transitions in the band structure of In_2S_3 has been drawn and illustrated in Figure S6(b), giving a very clear physical picture to understand the PL behavior of In_2S_3 .

Figure S7. The fitting curve for obtaining the optical bandgap from Figure 4(c).



The optical bandgap can be extracted by using Equation²³:

$$\alpha \propto (hv - E_g)^m/hv$$

where α is the effective absorption coefficient of a material, $h\nu$ is the photon energy, E_g is the bandgap of material, η (quantum efficiency) is a constant, the exponent $m = 2$ for indirect bandgap material and $1/2$ for direct bandgap material. By assuming that the internal quantum efficiency of photocurrent (I_{ph}) is a constant in the range from 550 to 650 nm, the photocurrent is proportional to the absorption in this wavelength range, i.e., $I_{ph} = \alpha \times \eta \times d$, where d is the thickness of the In_2S_3 nanoflake (here we assume the absorption rate $1 - e^{-\alpha d}$ as αd for ultrathin flakes)²⁴. Thus, we can obtain²³:

$$I_{ph} \propto (hv - E_g)^m/hv$$

Based on the above equations, the E_g is measured to be ≈ 2.04 eV under $m = 2$.

Figure S8. Spectrum response of NGs-In₂S₃ photodetectors with grating constants of (a) 300 nm and (b) 700 nm.

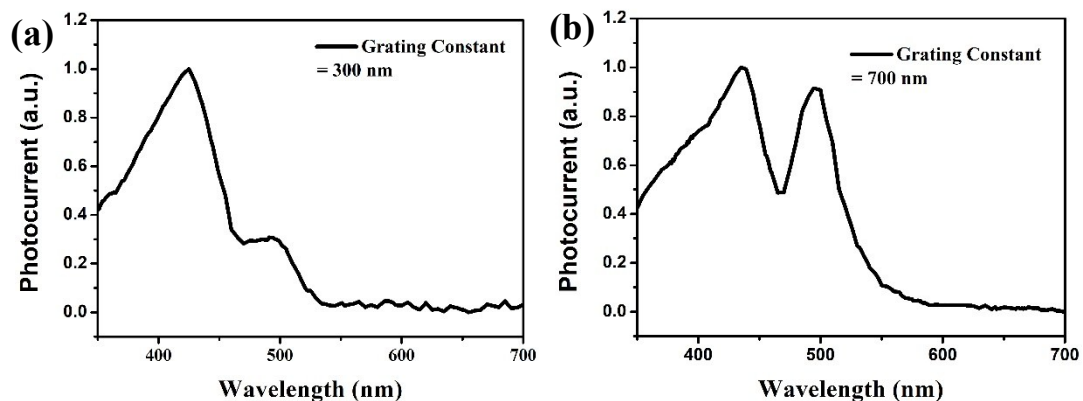


Figure S9. Bias voltage-dependent photocurrent of the NGs-In₂S₃ devices with various grating constants. The power density is 31.4 mW/cm². At the bias voltage of 2 V, the photocurrent of the NGs-In₂S₃ photodetector with a grating constant of 500 nm is 5390 nA. This value is 60 times higher than that of the device with a grating constant of 300 nm (89.2 nA). Meanwhile, this value (5390 nA) is 18.5 times higher than that of the device with a grating constant of 700 nm (292 nA).

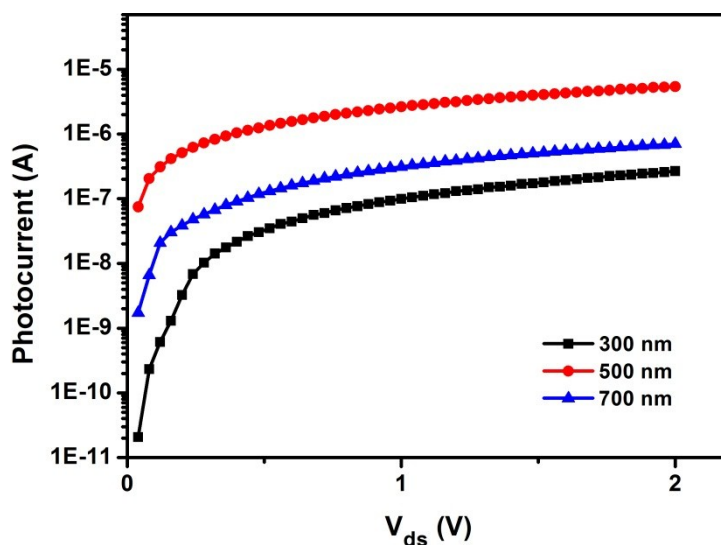


Figure S10. Schematic device structures of the (a) f-In₂S₃ and (b) NGs-In₂S₃. Comparison of I-V curves of the f-In₂S₃ and NGs-In₂S₃ photodetectors (c–d) in the dark, (e) under the same light illumination (405 nm, 31.4 mW/cm²).

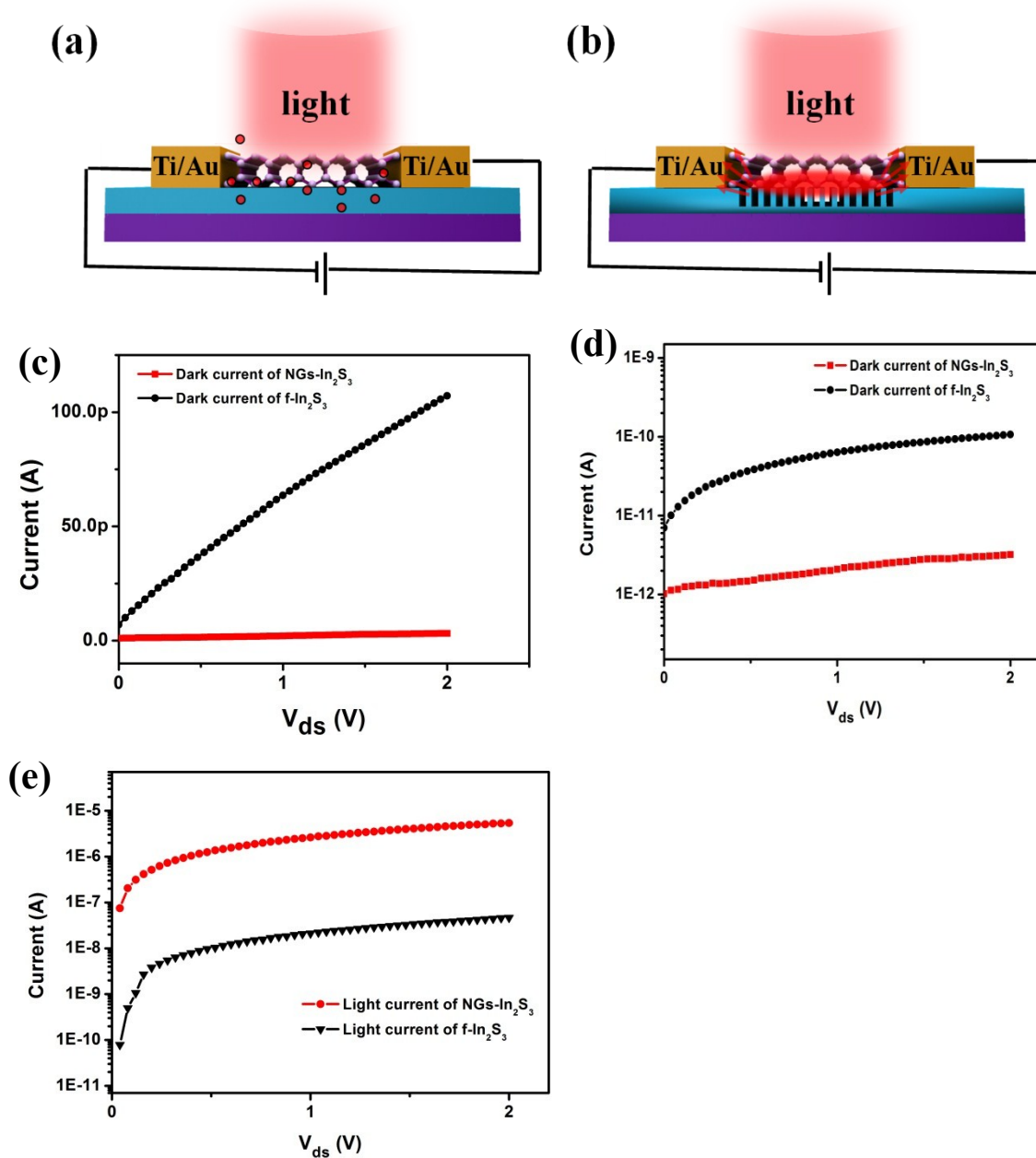


Figure S11. Light intensity dependent photocurrent (I_{ph}) of the f-In₂S₃ device under a bias of 2 V.

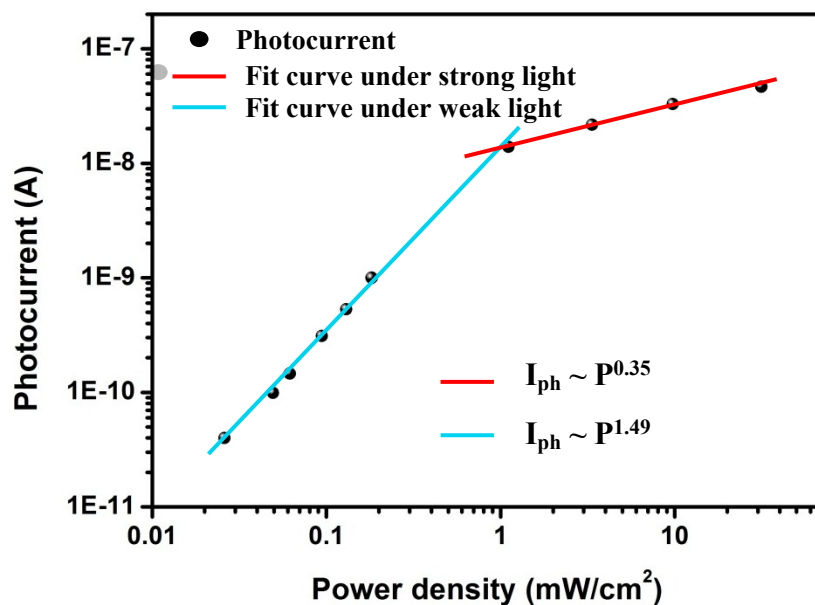


Figure S12. Light intensity dependent photoresponsivity (R) and detectivity (D*) of the f-In₂S₃ device under a bias of 2 V.

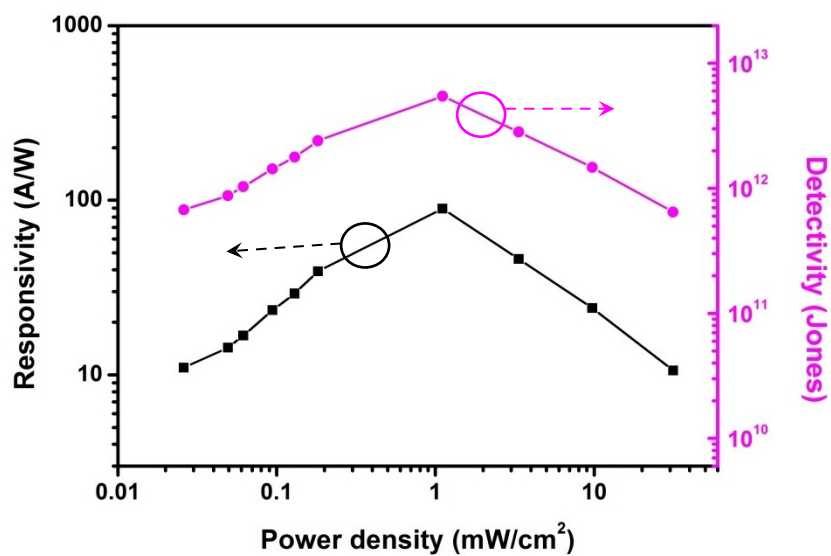


Figure S13. Light intensity dependent photoconductive gain of the f-In₂S₃ and NGs-In₂S₃ photodetectors under a bias of 2 V.

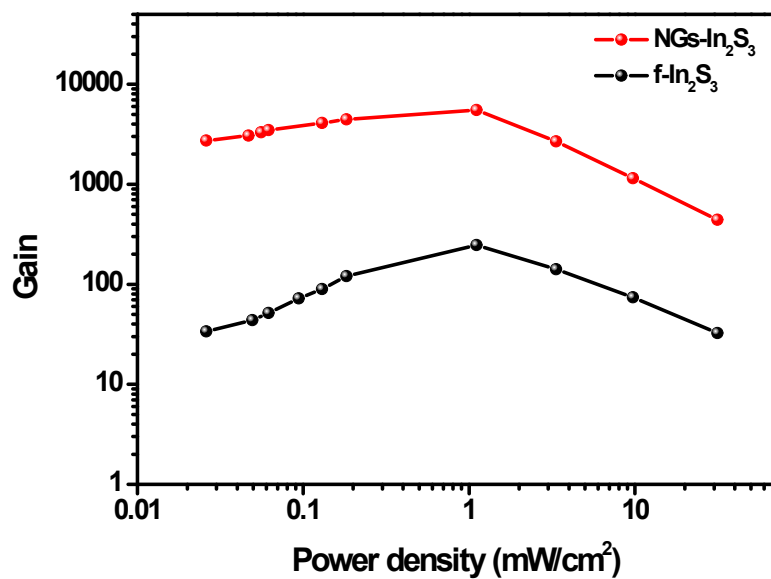
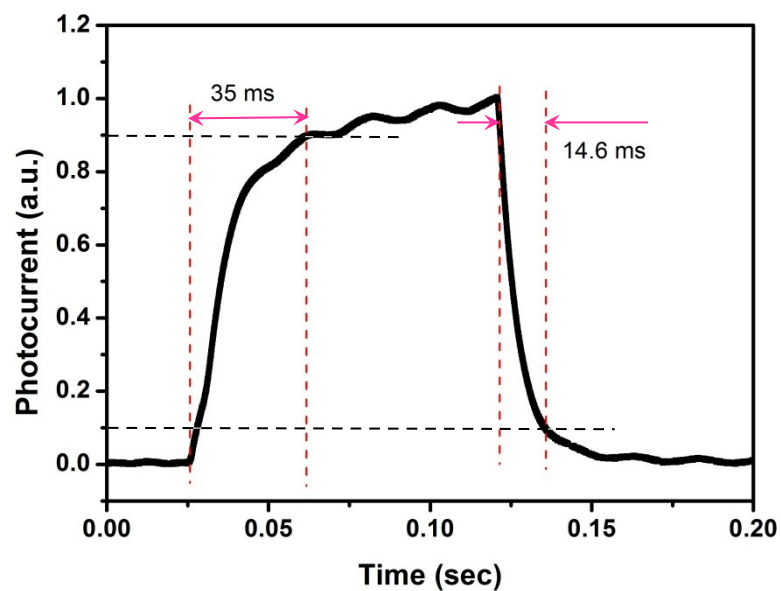


Figure S14. Dynamic response of photocurrent of the f-In₂S₃ device.



Supplementary Table

Table S1. Comparison of the key parameters of our NGs-In₂S₃ device with other non-layered 2D materials-based photodetectors. ND: no data.

Devices	R (A/W)	D* (Jones)	SNR	Gain	Rise/decay time (ms)	Ref.
NGs-In₂S₃	1810	2.09×10¹⁵	1.7×10⁶	5555	0.41/0.85	Ours
In₂S₃	137	7.74×10 ¹⁰	250	378	6/8	13
Bi₂O₂Se	6.5	8.3×10 ¹¹	~5	~10	2.8/4.5	9
CdTe	0.6	10 ⁹	27	1.6	18.4/14.7	25
SnTe	71	ND	~2	347	210/730	26
PbS	1621	10 ¹¹	~2	2512	300/300	3
Pb_{1-x}Sn_xSe	5.95	ND	~3	15.6	900/740	27
Te	160	ND	~3	420	4400/2800	28
CuBr	3.17	1.4×10 ¹¹	~200	11.3	32/48	4

Table S2. Comparison of the key parameters of our NGs-In₂S₃ device with other layered 2D materials-based photodetectors.

Devices	R (A/W)	D* (Jones)	SNR	Gain	Rise/decay time (ms)	Ref.
NGs-In₂S₃	1810	2.09×10¹⁵	1.7×10⁶	5555	0.41/0.85	Ours
SnSe₂	1100	10 ¹⁰	~10	2600	14.5/8.1	29
MoS₂	880	ND	~100	ND	4000/9000	30
WS₂	3.5	~10 ¹¹	54	8.1	ND	31
SnS₂	260	10 ¹⁰	10 ⁴	930	20/16	32
NiPS₃	0.126	1.22×10 ¹²	~100	0.61	3.2/15.6	33
InSe	27	ND	5	57	500/1700	34
In₂Se₃	395	2.26×10 ¹²	~10	1630	18/73	35
GaS	19.2	10 ¹⁴	~10 ⁴	20.5	30/30	36
GaSe	1.4	ND	~2	6	ND	37
GaTe	10 ⁴	ND	~5	23364	6/20	38
PtSe₂	4.5	7×10 ⁸	ND	ND	1.2/1.2	39

Table S3. Comparison of the key parameters of our NGs-In₂S₃ device with 2D materials heterojunction photodetectors. SWNT: single-walled carbon nanotube, Gr: graphene. As can be seen, although the obtained detectivity of our NGs-In₂S₃ device is slightly smaller than that of the CNT/ZnO heterostructure device, other parameters including photoresponsivity (1810 A/W versus 400 A/W), response time (0.41/0.85 ms versus 14000/23000 ms), SNR (1.7×10^6 versus 10^3) and dark current (3.2 pA versus 2000 pA) are much better. Therefore, the overall performance of our NGs-In₂S₃ device exceeds that of CNT/ZnO heterostructure device. Moreover, the photosensing material ZnO is up to 400 nm, which greatly hinders its application in wearable devices. In contrast, our work exploits a simple solution based on a single photosensing material. An ultrasensitive 2D In₂S₃ (just 19 nm in thickness) photodetector is achieved by adopting strain engineering coupled with optical regulation, which reflects the superiority of our solution. On the other hand, as for the In₂S₃/Gr/Si device, the double-heterojunction brings the photogating effect based on the photovoltaic effect. Therefore, the photoresponsivity of the In₂S₃/graphene/Si device is higher than our NGs-In₂S₃ device. However, constructing the double-heterojunction is based on artificial mechanical stacking techniques, which requires precise alignment. At the same time, the combination of three sensing materials makes the preparation process rather cumbersome. Our work uses only a single photosensing material to achieve an ultrasensitive 2D In₂S₃ photodetector by adopting strain engineering coupled with optical regulation. Due to the lack of photogating effect, the photoresponsivity is suppressed. But the formation of the built-in electric fields array makes SNR and D* much larger than those of the In₂S₃/graphene/Si device (1.7×10^6 versus 665.1 and 2.09×10^{15} Jones versus 3.02×10^{11} Jones). Moreover, our device is highly compatible with the photogating effect, which thus can be introduced to further improve the performance in the future.

Devices	R (A/W)	D* (Jones)	SNR	Gain	Rise/decay time (ms)	Ref.
NGs-In₂S₃	1810	2.09×10¹⁵	1.7×10⁶	5555	0.41/1.3	Ours
In₂S₃/Gr/Si	4.53×10 ⁴	3.02×10 ¹¹	665.1	1.4×10 ⁵	0.033/0.04	16
SWNT/ZnO	400	3.2×10 ¹⁵	~1000	ND	14000/23000	40
MoS₂/GaTe	21.83	8.4×10 ¹³	10 ³	57.3	7/7	41
MoS₂/WS₂	1173	4×10 ¹¹	~5	5460	>10 ³ /10 ³	42
WSe₂/GaSe	1000	2×10 ¹²	ND	2336	30/20	43
WSe₂/SnS₂	0.1	4.71×10 ¹⁰	ND	~0.3	0.5/0.6	44
WSe₂/SnS₂	244	1.29×10 ¹³	10 ⁶	551	13/24	45
Bi₂Te₃/Si	1	2.5×10 ¹²	~40	2.3	100/100	46
MoS₂/Si	11.9	2.1×10 ¹⁰	60	18.3	0.03/0.07	47
Gr/Si	0.73	4.2×10 ¹²	300	1	0.32/0.75	48
In₂Se₃/Si	5.9	4.9×10 ¹²	600	16.5	8.8/8.3	49
Bi/WS₂/Si	0.42	1.36×10 ¹³	10 ⁶	1	100/100	50

References

- (1) Zheng, Z.; Yao, J.; Yang, G. Self-Assembly of the Lateral In₂Se₃/CuInSe₂ Heterojunction for Enhanced Photodetection. *ACS Appl. Mater. Interfaces* **2017**, *9* (8), 7288-7296.
- (2) Fu, L.; Wang, F.; Wu, B.; Wu, N.; Huang, W.; Wang, H.; Jin, C.; Zhuang, L.; He, J.; Fu, L.; Liu, Y. Van der Waals Epitaxial Growth of Atomic Layered HfS₂ Crystals for Ultrasensitive Near-Infrared Phototransistors. *Adv. Mater.* **2017**, *29* (32), 1700439.
- (3) Wen, Y.; Wang, Q.; Yin, L.; Liu, Q.; Wang, F.; Wang, F.; Wang, Z.; Liu, K.; Xu, K.; Huang, Y.; Shifa, T. A.; Jiang, C.; Xiong, J.; He, J. Epitaxial 2D PbS Nanoplates Arrays with Highly Efficient Infrared Response. *Adv. Mater.* **2016**, *28* (36), 8051-8057.
- (4) Gong, C.; Chu, J.; Yin, C.; Yan, C.; Hu, X.; Qian, S.; Hu, Y.; Hu, K.; Huang, J.; Wang, H.; Wang, Y.; Wangyang, P.; Lei, T.; Dai, L.; Wu, C.; Chen, B.; Li, C.; Liao, M.; Zhai, T.; Xiong, J. Self-Confined Growth of Ultrathin 2D Nonlayered Wide-

- Bandgap Semiconductor CuBr Flakes. *Adv. Mater.* **2019**, *31* (36), 1903580.
- (5) Su, G.; Hadjiev, V. G.; Loya, P. E.; Zhang, J.; Lei, S.; Maharjan, S.; Dong, P.; P, M. A.; Lou, J.; Peng, H. Chemical vapor deposition of thin crystals of layered semiconductor SnS₂ for fast photodetection application. *Nano Lett.* **2015**, *15* (1), 506-513.
- (6) Fu, Q.; Zhu, C.; Zhao, X.; Wang, X.; Chaturvedi, A.; Zhu, C.; Wang, X.; Zeng, Q.; Zhou, J.; Liu, F.; Tay, B. K.; Zhang, H.; Pennycook, S. J.; Liu, Z. Ultrasensitive 2D Bi₂O₂Se Phototransistors on Silicon Substrates. *Adv. Mater.* **2019**, *31* (1), 1804945.
- (7) Deng, W.; Zhang, X.; Huang, L.; Xu, X.; Wang, L.; Wang, J.; Shang, Q.; Lee, S. T.; Jie, J. Aligned Single-Crystalline Perovskite Microwire Arrays for High-Performance Flexible Image Sensors with Long-Term Stability. *Adv. Mater.* **2016**, *28* (11), 2201-2208.
- (8) Li, A.; Chen, Q.; Wang, P.; Gan, Y.; Qi, T.; Wang, P.; Tang, F.; Wu, J. Z.; Chen, R.; Zhang, L.; Gong, Y. Ultrahigh-Sensitive Broadband Photodetectors Based on Dielectric Shielded MoTe₂/Graphene/SnS₂ p-g-n Junctions. *Adv. Mater.* **2018**, *31* (6), 1805656.
- (9) Li, J.; Wang, Z.; Wen, Y.; Chu, J.; Yin, L.; Cheng, R.; Lei, L.; He, P.; Jiang, C.; Feng, L.; He, J. High-Performance Near-Infrared Photodetector Based on Ultrathin Bi₂O₂Se Nanosheets. *Adv. Funct. Mater.* **2018**, *28* (10), 1706437.
- (10) Wei, Y.; Ren, Z.; Zhang, A.; Mao, P.; Li, H.; Zhong, X.; Li, W.; Yang, S.; Wang, J. Hybrid Organic/PbS Quantum Dot Bilayer Photodetector with Low Dark Current and High Detectivity. *Adv. Funct. Mater.* **2018**, *28* (11), 1706690.
- (11) Xie, C.; Mak, C.; Tao, X.; Yan, F. Photodetectors Based on Two-Dimensional Layered Materials Beyond Graphene. *Adv. Funct. Mater.* **2016**, *27* (19), 1603886.
- (12) Long, M.; Wang, P.; Fang, H.; Hu, W. Progress, Challenges, and Opportunities for 2D Material Based Photodetectors. *Adv. Funct. Mater.* **2018**, *29* (19), 1803807.
- (13) Huang, W.; Gan, L.; Yang, H.; Zhou, N.; Wang, R.; Wu, W.; Li, H.; Ma, Y.; Zeng, H.; Zhai, T. Controlled Synthesis of Ultrathin 2D β-In₂S₃ with Broadband Photoresponse by Chemical Vapor Deposition. *Adv. Funct. Mater.* **2017**, *27* (36), 1702448.

- (14) Li, B.; Huang, L.; Zhong, M. Z.; Li, Y.; Wang, Y.; Li, J. B.; Wei, Z. M. Direct Vapor Phase Growth and Optoelectronic Application of Large Band Offset SnS₂/MoS₂ Vertical Bilayer Heterostructures with High Lattice Mismatch. *Adv. Electron. Mater.* **2016**, *2* (11), 1600298.
- (15) Li, Y. T.; Wang, Y.; Huang, L.; Wang, X. T.; Li, X. Y.; Deng, H. X.; Wei, Z. M.; Li, J. B. Anti-Ambipolar Field-Effect Transistors Based On Few-Layer 2D Transition Metal Dichalcogenides. *ACS Appl. Mater. Interfaces* **2016**, *8* (24), 15574-15581.
- (16) Lu, J.; Zheng, Z.; Yao, J.; Gao, W.; Zhao, Y.; Xiao, Y.; Li, J. 2D In₂S₃ Nanoflake Coupled with Graphene toward High-Sensitivity and Fast-Response Bulk-Silicon Schottky Photodetector. *Small* **2019**, *15* (47), 1904912.
- (17) Ho, C. H.; Wang, Y. P.; Chan, C. H.; Huang, Y. S.; Li, C. H. Temperature-dependent photoconductivity in beta-In₂S₃ single crystals. *J. Appl. Phys.* **2010**, *108* (4), 043518.
- (18) Mathew, M.; Jayakrishnan, R.; Kumar, P. M. R.; Kartha, C. S.; Vijayakumar, K. P.; Kashiwaba, Y.; Abe, T. Anomalous behavior of silver doped indium sulfide thin films. *J. Appl. Phys.* **2006**, *100* (3), 033504.
- (19) Pai, R. R.; John, T. T.; Kashiwaba, Y.; Abe, T.; Vijayakumar, K. P.; Kartha, C. S. Defect characterization of spray pyrolysed β-In₂S₃ thin film using thermally stimulated current measurements. *J. Mater. Sci.* **2005**, *40* (3), 741-746.
- (20) Jayakrishnan, R.; Sebastian, T.; Kartha, C. S.; Vijayakumar, K. P. Effect of defect bands in β-In₂S₃ thin films. *J. Appl. Phys.* **2012**, *111* (9), 093714.
- (21) Ho, C. H. Growth and characterization of near-band-edge transitions in β-In₂S₃ single crystals. *J. Cryst. Growth* **2010**, *312* (19), 2718-2723.
- (22) Ghorbani, E.; Albe, K. Intrinsic point defects in β-In₂S₃ studied by means of hybrid density-functional theory. *J. Appl. Phys.* **2018**, *123* (10), 103103.
- (23) Lei, S. D.; Ge, L. H.; Najmaei, S.; George, A.; Kappera, R.; Lou, J.; Chhowalla, M.; Yamaguchi, H.; Gupta, G.; Vajtai, R.; Mohite, A. D.; Ajayan, P. M. Evolution of the Electronic Band Structure and Efficient Photo-Detection in Atomic Layers of InSe. *Acs Nano* **2014**, *8* (2), 1263-1272.
- (24) Zhou, X.; Gan, L.; Tian, W. M.; Zhang, Q.; Jin, S. Y.; Li, H. Q.; Bando, Y.;

Golberg, D.; Zhai, T. Y. Ultrathin SnSe₂ Flakes Grown by Chemical Vapor Deposition for High-Performance Photodetectors. *Adv. Mater.* **2015**, *27* (48), 8035-8041.

(25) Cheng, R.; Wen, Y.; Yin, L.; Wang, F.; Wang, F.; Liu, K.; Shifa, T. A.; Li, J.; Jiang, C.; Wang, Z.; He, J. Ultrathin Single-Crystalline CdTe Nanosheets Realized via Van der Waals Epitaxy. *Adv. Mater.* **2017**, *29* (35), 1703122.

(26) Yang, J.; Yu, W.; Pan, Z.; Yu, Q.; Yin, Q.; Guo, L.; Zhao, Y.; Sun, T.; Bao, Q.; Zhang, K. Ultra-Broadband Flexible Photodetector Based on Topological Crystalline Insulator SnTe with High Responsivity. *Small* **2018**, *14* (37), 1802598.

(27) Wang, Q.; Xu, K.; Wang, Z.; Wang, F.; Huang, Y.; Safdar, M.; Zhan, X.; Wang, F.; Cheng, Z.; He, J. Van Der Waals Epitaxial Ultrathin Two-dimensional Nonlayered Semiconductor for Highly Efficient Flexible Optoelectronic Devices. *Nano Lett.* **2015**, *15* (2), 1183-1189.

(28) Wang, Q.; Safdar, M.; Xu, K.; Mirza, M.; Wang, Z.; He, J. Van der Waals Epitaxy and Photoresponse of Hexagonal Tellurium Nanoplates on Flexible Mica Sheets. *ACS Nano* **2014**, *8* (7), 7497-7505.

(29) Zhou, X.; Gan, L.; Tian, W.; Zhang, Q.; Jin, S.; Li, H.; Bando, Y.; Golberg, D.; Zhai, T. Ultrathin SnSe₂ Flakes Grown by Chemical Vapor Deposition for High-Performance Photodetectors. *Adv. Mater.* **2015**, *27* (48), 8035-8041.

(30) Lopez-Sanchez, O.; Lembke, D.; Kayci, M.; Radenovic, A.; Kis, A. Ultrasensitive Photodetectors Based on Monolayer MoS₂. *Nat. Nanotechnol.* **2013**, *8* (7), 497-501.

(31) Tan, H.; Fan, Y.; Zhou, Y.; Chen, Q.; Xu, W.; Warner, J. H. Ultrathin 2D Photodetectors Utilizing Chemical Vapor Deposition Grown WS₂ With Graphene Electrodes. *ACS Nano* **2016**, *10* (8), 7866-7873.

(32) Hafeez, M.; Gan, L.; Li, H.; Ma, Y.; Zhai, T. Large-Area Bilayer ReS₂ Film/Multilayer ReS₂ Flakes Synthesized by Chemical Vapor Deposition for High Performance Photodetectors. *Adv. Funct. Mater.* **2016**, *26* (25), 4551-4560.

(33) Chu, J.; Wang, F.; Yin, L.; Lei, L.; Yan, C.; Wang, F.; Wen, Y.; Wang, Z.; Jiang, C.; Feng, L.; Xiong, J.; Li, Y.; He, J. High-Performance Ultraviolet Photodetector

Based on a Few-Layered 2D NiPS₃ Nanosheet. *Adv. Funct. Mater.* **2017**, *27* (32), 1701342.

(34) Yang, Z.; Jie, W.; Mak, C.-H.; Lin, S.; Lin, H.; Yang, X.; Yan, F.; Lau, S. P.; Hao, J. Wafer-Scale Synthesis of High-Quality Semiconducting Two-Dimensional Layered InSe with Broadband Photoresponse. *ACS Nano* **2017**, *11* (4), 4225-4236.

(35) Jacobs-Gedrim, R. B.; Shanmugam, M.; Jain, N.; Durcan, C. A.; Murphy, M. T.; Murray, T. M.; Matyi, R. J.; Moore, R. L., 2nd; Yu, B. Extraordinary Photoresponse in Two-dimensional In₂Se₃ Nanosheets. *ACS Nano* **2014**, *8* (1), 514-521.

(36) Hu, P.; Wang, L.; Yoon, M.; Zhang, J.; Feng, W.; Wang, X.; Wen, Z.; Idrobo, J. C.; Miyamoto, Y.; Geohegan, D. B.; Xiao, K. Highly Responsive Ultrathin GaS Nanosheet Photodetectors on Rigid and Flexible Substrates. *Nano Lett.* **2013**, *13* (4), 1649-1654.

(37) Mahjouri-Samani, M.; Gresback, R.; Tian, M.; Wang, K.; Puretzky, A. A.; Rouleau, C. M.; Eres, G.; Ivanov, I. N.; Xiao, K.; McGuire, M. A.; Duscher, G.; Geohegan, D. B. Pulsed Laser Deposition of Photoresponsive Two-Dimensional GaSe Nanosheet Networks. *Adv. Funct. Mater.* **2014**, *24* (40), 6365-6371.

(38) Liu, F.; Shimotani, H.; Shang, H.; Kanagasekaran, T.; Zolyomi, V.; Drummond, N.; Fal'ko, V. I.; Tanigaki, K. High-sensitivity Photodetectors Based on Multilayer GaTe flakes. *ACS Nano* **2014**, *8* (1), 752-760.

(39) Yu, X.; Yu, P.; Wu, D.; Singh, B.; Zeng, Q.; Lin, H.; Zhou, W.; Lin, J.; Suenaga, K.; Liu, Z.; Wang, Q. J. Atomically thin Noble Metal Dichalcogenide: a Broadband Mid-infrared Semiconductor. *Nat. Commun.* **2018**, *9* (1), 1-9.

(40) Li, G.; Suja, M.; Chen, M.; Bekyarova, E.; Haddon, R. C.; Liu, J.; Itkis, M. E. Visible-Blind UV Photodetector Based on Single-Walled Carbon Nanotube Thin Film/ZnO Vertical Heterostructures. *ACS Appl. Mater. Interfaces* **2017**, *9* (42), 37094-37104.

(41) Wang, F.; Wang, Z.; Xu, K.; Wang, F.; Wang, Q.; Huang, Y.; Yin, L.; He, J. Tunable GaTe-MoS₂ van der Waals p-n Junctions with Novel Optoelectronic Performance. *Nano Lett.* **2015**, *15* (11), 7558-7566.

(42) Tan, H.; Xu, W.; Sheng, Y.; Lau, C. S.; Fan, Y.; Chen, Q.; Tweedie, M.; Wang,

X.; Zhou, Y.; Warner, J. H. Lateral Graphene-Contacted Vertically Stacked WS₂/MoS₂ Hybrid Photodetectors with Large Gain. *Adv. Mater.* **2017**, *29* (46), 1702917.

(43) Yang, Z.; Liao, L.; Gong, F.; Wang, F.; Wang, Z.; Liu, X.; Xiao, X.; Hu, W.; He, J.; Duan, X. WSe₂/GeSe Heterojunction Photodiode with Giant Gate Tunability. *Nano Energy* **2018**, *49*, 103-108.

(44) Yang, T.; Zheng, B.; Wang, Z.; Xu, T.; Pan, C.; Zou, J.; Zhang, X.; Qi, Z.; Liu, H.; Feng, Y.; Hu, W.; Miao, F.; Sun, L.; Duan, X.; Pan, A. Van der Waals epitaxial growth and optoelectronics of large-scale WSe₂/SnS₂ vertical bilayer p-n junctions. *Nat. Commun.* **2017**, *8* (1), 1906.

(45) Zhou, X.; Hu, X.; Zhou, S.; Song, H.; Zhang, Q.; Pi, L.; Li, L.; Li, H.; Lü, J.; Zhai, T. Tunneling Diode Based on WSe₂/SnS₂ Heterostructure Incorporating High Detectivity and Responsivity. *Adv. Mater.* **2018**, *30* (7), 1703286.

(46) Yao, J.; Shao, J.; Wang, Y.; Zhao, Z.; Yang, G. Ultra-broadband and High Response of the Bi₂Te₃-Si Heterojunction and its Application as a Photodetector at Room Temperature in Harsh Working Environments. *Nanoscale* **2015**, *7* (29), 12535-12541.

(47) Zhang, Y.; Yu, Y.; Mi, L.; Wang, H.; Zhu, Z.; Wu, Q.; Zhang, Y.; Jiang, Y. In Situ Fabrication of Vertical Multilayered MoS₂/Si Homotype Heterojunction for High-Speed Visible-Near-Infrared Photodetectors. *Small* **2016**, *12* (8), 1062-1071.

(48) Li, X.; Zhu, M.; Du, M.; Lv, Z.; Zhang, L.; Li, Y.; Yang, Y.; Yang, T.; Li, X.; Wang, K.; Zhu, H.; Fang, Y. High Detectivity Graphene-Silicon Heterojunction Photodetector. *Small* **2016**, *12* (5), 595-601.

(49) Zheng, Z.; Yao, J.; Wang, B.; Yang, Y.; Yang, G.; Li, J. Self-Assembly High-Performance UV-vis-NIR Broadband beta-In₂Se₃/Si Photodetector Array for Weak Signal Detection. *ACS Appl. Mater. Interfaces* **2017**, *9* (50), 43830-43837.

(50) Yao, J.; Zheng, Z.; Shao, J.; Yang, G. Promoting Photosensitivity and Detectivity of the Bi/Si Heterojunction Photodetector by Inserting a WS₂ Layer. *ACS Appl. Mater. Interfaces* **2015**, *7* (48), 26701-26708.